Continental Shelf Research 30 (2010) 226–238

Contents lists available at ScienceDirect

Continental Shelf Research

journal homepage: www.elsevier.com/locate/csr

Nearshore bar migration and sediment-induced buoyancy effects

Silvia Falchetti [a,*], Daniel C. Conley [b], Maurizio Brocchini [c], Steve Elgar [d]

[a] Dipartimento di Ingegneria delle Costruzioni, dell'Ambiente e del Territorio, Università di Genova, Via Montallegro 1, 16145, Genova, Italy
[b] Marine Institute, University of Plymouth, Portland Square A504, Drake Circus, Plymouth PL48AA, Devon, UK
[c] Dipartimento di Idraulica, Strade, Ambiente e Chimica, Università Politecnica delle Marche, Via Brecce Bianche 12, 60131 Ancona, Italy
[d] Woods Hole Oceanographic Institution, MS#11, Woods Hole, MA 02543, USA

ARTICLE INFO

Article history:
Received 6 February 2009
Received in revised form
3 November 2009
Accepted 16 November 2009
Available online 24 November 2009

Keywords:
Nearshore bars
Boundary layers
Sediment transport
Stratified flow
Buoyancy

ABSTRACT

A 1-D General Ocean Turbulence Model that includes the effects of sediment-induced stratification is shown to simulate the observed onshore and offshore migration of a nearshore sandbar. The only two free parameters of the model, the bed reference concentration and the sediment diffusivity, are taken from the literature, rather than tuned to the data used here. The model results suggest that predictions of onshore bar migration, in which wave-induced sediment transport confined to within a few centimeters of the bottom dominates, are not greatly affected by accounting for buoyancy effects. The model results also suggest that both mean flows and waves transport sediment during offshore bar migration, with different components of transport dominating at different cross-shore locations across the bar-trough bathymetry. Neglecting the effects of sediment-induced stratification results in higher model skill during the largest waves, likely because the excess turbulence production simulated by the non-stratified model is counterbalanced by neglected breaking-wave-generated turbulence. Considering both onshore and offshore migration, the model that includes sediment-induced stratification has higher skill than the model without stratification.

1. Introduction

There are many models for sediment transport and subsequent sandbar migration near the shoreline. Some parametric sediment transport models are based on an "energetics" approach (Bagnold, 1966) that relates the sediment transport rate for steady flows to the rate of work on the bed by near-bottom currents. Energetics models have been extended to account for the combined wave-induced and mean current-driven transport near the shoreline (Bowen, 1980; Bailard, 1981; Bailard and Inman, 1981, hereinafter BBB), and have been compared with field observations (Thornton et al., 1996; Gallagher et al., 1998). BBB-based models predict the offshore migration of sandbars observed during storms, but fail to predict the corresponding development of the bar trough and the onshore migration observed during less energetic conditions (Thornton et al., 1996; Gallagher et al., 1998).

A model that accounts for nonlinear wave boundary layer processes (Trowbridge and Young, 1989) reproduces an onshore sandbar migration event observed on a natural beach outside of the surf zone, but fails to predict seaward bar migration, probably owing to the exclusion of sediment transport by offshore-directed mean currents (undertow).

Motivated by the inability of BBB models to reproduce onshore sediment transport during moderate wave conditions, a model (Hoefel and Elgar, 2003) that parameterizes the effects of fluid acceleration on the bed load transport for highly unsteady flows (Drake and Calantoni, 2001) was developed. The inclusion of a term for acceleration-driven transport results in skillful predictions of onshore bar migration and improved skill for predicting offshore migration (Hoefel and Elgar, 2003).

More recently, a model that includes the effects of alongshore currents (Plant et al., 2004) was shown to predict both the onshore and offshore bar migration observed on the same ocean beach investigated here. However, skillful predictions required tuning of several free parameters using inverse objective methods.

An alternative approach is based on wave-resolving, eddy-diffusive modeling (Henderson et al., 2004; Hsu et al., 2006). These models include nonlinear wave boundary layer processes in the determination of the shoreward sediment motion. For example, wave-generated momentum fluxes and Stokes drift are necessary to reproduce the observed shoreward transport (Henderson et al., 2004). Although the model predicts both onshore and offshore bar migration, at least two tunable parameters were varied over all individual simulations. Similarly, to simulate the observed onshore migration, the roughness height used in a bottom boundary layer model was increased with respect to that used in the case of a clear fluid, with two different

* Corresponding author. Tel.: +39 0187 527318; fax: +39 0187 527354.
E-mail address: falchetti@nurc.nato.int (S. Falchetti).

0278-4343/$ - see front matter © 2009 Elsevier Ltd. All rights reserved.
doi:10.1016/j.csr.2009.11.005

values used depending on the chosen turbulence scheme (Hsu et al., 2006). Based on results from phase-resolving models, a modified version of the BBB model with different friction factors for oscillatory-only and mean-plus-oscillatory-flow-driven transport was developed (Hsu et al., 2006). This new wave-averaged energetics-type model has better skill reproducing onshore bar migration than is obtained with the standard energetics model (BBB).

Although there is almost universal agreement that the mean offshore-directed currents (undertow) dominate the seaward movement of the sandbar, the mechanisms of onshore sediment transport and bar migration are not fully understood. Boundary layer streaming, fluid accelerations, plug flows (Foster et al., 2006), and variable friction factors may be important. These phenomena tend to be parameterized by adjustable coefficients in many models.

Here, a new approach is investigated. Specifically, a 1-D General Ocean Turbulence Model (GOTM, Burchard et al., 1998, 1999) that includes the effects of sediment-induced stratification is shown to simulate the observed onshore and offshore migration of a nearshore sandbar. Stratification owing to strong upwardly diminishing sediment concentration gradients can enhance the role of near-bed transport by limiting the dispersion of sediment farther into the water column (Conley et al., 2008), resulting in a reduction in the contribution of the mean sediment transport from suspended sediments higher in the water column and an increase in the coherent transport that is biased toward the onshore directed high-velocity peaks under wave crests. The model is used here to investigate the role of an increase in the coherent transport component close to the bed on sandbar migration, and demonstrates the importance of sediment-induced buoyancy effects to sediment transport and morphological change in the surf zone. The model contains two free parameters, which affect the bed reference concentration and the sediment diffusivity, respectively. For the application discussed here, these parameters are determined independently of the observed bar migration events, and kept constant for all wave conditions.

Nonlinear wave boundary layer processes are not included in the model explicitly, but nearbed flow dynamics are partially accounted for by the high-resolution discretization of the computed flow near the bottom. Moreover, during storms when sediment-induced stratification is expected to be maximum (Glenn and Grant, 1987; Styles and Glenn, 2000) neglect of boundary layer streaming does not reduce model skill (Thornton et al., 1996; Gallagher et al., 1998, Hsu et al., 2006).

The model is described first, followed by an analysis of the field observations. Comparisons of model predictions with observations are presented next, followed by a discussion of the results.

2. The numerical model

Numerical simulations that include the effects of sediment-stratified bottom boundary layers were performed using a modified form of the sediment transport component of the 1-D General Ocean Turbulence Model (GOTM) (Burchard et al., 1998; Umlauf et al., 2006), an open source, two-equation (k–ε) turbulence closure model based on the hydrodynamic equations of motion. The model uses the Boussinesq (density only considered variable when multiplied by the gravitational acceleration), hydrostatic, and eddy viscosity approximations, and has been used in a wide range of applications (Blackford et al., 2004; Stips et al., 2002; Ralston and Stacey, 2006). To simulate wave boundary sedimentary processes, the code has been modified to operate with sub-second time steps.

Here, a brief description of the complete model equations (Conley et al., 2008) necessary to understand the feedback between sediment load and flow is presented. The model can account for buoyancy fluxes, which have a direct influence on the turbulence dynamics, via the Brunt–Väisälä frequency N:

$$N=\sqrt{\frac{\partial}{\partial z}\left[-g\frac{\rho-\rho_0}{\rho_0}\right]} \tag{1}$$

where z is the vertical coordinate, ρ is the density of the sediment-laden fluid, ρ_0 is the density of clear water, and g is gravitational acceleration.

The turbulent kinetic energy (TKE) equation is

$$\frac{\partial k}{\partial t}-\frac{\partial}{\partial z}\left[(v_t)\frac{\partial k}{\partial z}\right]=v_tM^2-\mu_tN^2-\varepsilon \tag{2}$$

where k is the turbulent kinetic energy, t is time, v_t is the eddy viscosity, and M is the shear frequency, given by

$$M=\sqrt{\left(\frac{\partial u}{\partial z}\right)^2+\left(\frac{\partial v}{\partial z}\right)^2} \tag{3}$$

where u and v are cross- and alongshore components of the velocity, μ_t is the eddy diffusivity for passive tracers, and ε is the dissipation rate, given by

$$\frac{\partial \varepsilon}{\partial t}-\frac{\partial}{\partial z}\left[\mu_\varepsilon\frac{\partial \varepsilon}{\partial z}\right]=\frac{\varepsilon}{k}(1.44v_tM^2+\mu_\varepsilon N^2-1.92\varepsilon) \tag{4}$$

The eddy diffusivity for dissipation, μ_{ε}, is set equal to $\mu_t/1.08$ (e.g. Burchard et al., 1998).

2.1. The sediment transport model

To clarify the effects of sediment stratification, the sediment load is represented by suspended load only. Although neglecting bedload will affect overall model skill, it should not change the differences between stratified and nonstratified results, nor the conclusions. The conservation equation for the mass of suspended sediment accounts only for a diffusion process, assuming zero local horizontal advective flux:

$$\frac{\partial C}{\partial t}+\frac{\partial(w_sC)}{\partial z}=\frac{\partial}{\partial z}\left(\mu_s\frac{\partial C}{\partial z}\right) \tag{5}$$

where C is the sediment concentration, w_s is the settling velocity, and μ_s is the sediment diffusivity. The reference concentration, C_0, located directly at the bottom (i.e. z=0), is calculated by means of a Dirichlet boundary condition, which is a function of the actual bed shear velocity, u_{*b}, and of the critical bed shear velocity, u_{*c}:

$$C_0=\gamma[(u_{*b}/u_{*c})^2-1] \tag{6}$$

where γ is the first non-dimensional calibration parameter.

To solve Eq. (5), the Rouse equation is used to define a Dirichlet boundary condition for the sediment concentration C_b, which is located at the center of the lowest layer:

$$C_b=C_0\left[\frac{z+z_0}{z_0}\frac{h-z_0}{h-(z+z_0)}\right]^{-b};\quad b=\frac{w_s}{\kappa u_{*b}} \tag{7}$$

where h is the water depth, b is the Rouse number, z_0 is the bottom roughness, and κ is the Von Karman constant.

Assuming hydrodynamically rough flows, the bottom roughness reduces to:

$$z_0=0.03h_0+z_a \tag{8}$$

where h_0 is the Nikuradse roughness (equal to 2.5 times the grain diameter) and z_a is the sediment transport component, given by

(Nielsen, 1992)

$$z_a = 5.67\sqrt{u_{*_b}^2 - 0.05 g' D_{50}}\sqrt{\frac{D_{50}}{g'}} \tag{9}$$

where g' is the reduced gravity ($g(\rho_s-\rho_0)/\rho_0$), and D_{50} is the representative sediment size. This formulation for the roughness height was selected to incorporate a dependence on the sediment load. The model results and corresponding conclusions about the effects of stratification on sediment transport and sandbar migration are not sensitive to the details of the roughness. However, to calibrate the model under constant roughness conditions a value similar to the mean of the variable values obtained from Eq. (9) must be utilized.

The turbulent mixing of sediment μ_s is expressed as

$$\mu_s = \beta C_{\mu s}\frac{k^2}{\varepsilon}; \quad C_{\mu s} = \frac{C_\mu}{Pr_t} \tag{10}$$

where β is an adjustable, calibration constant that represents the mean ratio between the passive tracer diffusivity and the diffusivity of sediment (Nielsen and Teakle, 2004). The stability function used for passive tracer diffusivity, $C_{\mu s}$, is a function of the turbulent Prandtl number Pr_t, and the momentum stability function C_μ. Many different sets of stability functions have been proposed, all of which increase mixing in the case of unstable stratifications and decrease mixing for stable stratifications. Here, C_μ is taken as constant (0.5562) as in the k–ε literature (Rodi, 1980, 1987). The stability function for passive tracers is related to the Richardson number through the Prandtl number (Munk and Anderson, 1948):

$$Pr_t = \begin{cases} Pr_{0t}\dfrac{(1+3.33Ri)^{3/2}}{(1+10Ri)^{1/2}}, & \text{for } Ri \geq 0, \\ Pr_{0t} & \text{for } Ri < 0 \end{cases} \tag{11}$$

where Pr_{0t} is a turbulent constant Prandtl number for neutral stratification and Ri is the gradient Richardson number. For all the simulations presented, the reductive β parameter of Eq. (10) and the bottom concentration parameter γ of Eq. (6) have been fixed based on previous results (Smith and McLean, 1977; Conley et al., 2008). For the simulations including the effects of sediment buoyancy (SIS) they are fixed at the values of β=0.55 and $\gamma_1 = 1.54\times10^{-3}$. Solutions ignoring the effects of buoyancy (NSS) use the same values for β, with either the same value of γ_1, or with a reduced reference concentration parameter $\gamma_2 = 1.20\times10^{-3}$, which has been shown to be more appropriate when matching observed concentrations for the NSS solutions (Conley et al., 2008).

2.2. Shear velocity calculation and numerical grid

In GOTM the shear velocity is determined by means of a logarithmic profile:

$$u_{*_b} = \kappa/\log\left[\frac{z_0+z_1/2}{z_0}\right]\sqrt{u(1)^2+v(1)^2} \tag{12}$$

Measurements suggest that, for steady flow conditions, the fluid velocity profile just above the bed follows a logarithmic law (Sumer et al., 1996). For oscillatory boundary layers the viability of the assumption of a logarithmic velocity distribution at all phases of the flow depends on the value of the Nikuradse roughness normalized by the orbital wave amplitude (Nielsen, 1992). Even if the assumption of a constant shape of the velocity distribution for the different phases in the free-stream velocity is not always satisfied (especially during flow reversal) (Jensen et al., 1989), the ensuing scaling rules still may be appropriate. The application of the log law is common, and can be found in studies such as open-channel flows subjected to stratification (Hsu et al., 2003), and onshore bar migration simulated with a wave-resolving model (Henderson et al., 2004).

The first point of the grid z_1 is taken at 0.5 cm, consistent with the maximum roughness length equal to 4 mm (20 D_{50}). A spacing interval of 1.5 mm was used for the first 100 points of the domain above the bed, followed by a grid spacing increasing up to the surface, for a total of 150 points.

3. The field data

The model predictions of sandbar migration are compared with the patterns of erosion and accretion observed on an ocean beach on the Outer Banks of North Carolina (Gallagher et al., 1998; Elgar et al., 2001). Although results are presented for a 45-day period from 1 September to 15 October 1994, focus is on single bar migration events analyzed previously (Gallagher et al., 1998; Elgar et al., 2001; Hoefel and Elgar, 2003; Henderson et al., 2004). Using terminology previously introduced (Gallagher et al., 1998), three cases of offshore migration (labeled 'a', 'c', and 'd', respectively), and one case of onshore migration (labeled 'b') are investigated in detail.

3.1. Environmental conditions

The environmental conditions characterizing the 4 events are shown in Fig. 1 and described below.

Event 'a' occurred between 1 and 5 September at 19:00 h. The environmental conditions characterizing this event are shown in Fig. 1. The waves in this period were energetic, with the significant wave height observed in 4 m depth reaching a maximum of 2.5 m at the peak of the storm. The sandbar migrated about 50 m offshore during this period.

Event 'b' occurred between 22 and 27 September at 19:00 h. Incident waves were moderately energetic, with the significant wave height in 4 m depth slowly diminishing from a peak of 1.3 m to a minimum of 0.1 m at mid-day of the 25th, and then increasing briefly to a secondary peak of 1.2 m. The sandbar migrated approximately 20 m onshore during this period.

Event 'c' occurred between 2 and 4 October at 16:00 h. During this period the wave height increased from about 0.5 to 2.5 m, and then decreased to 0.5 m at the end of the period. The sandbar migrated approximately 20 m offshore during this period.

Event 'd' occurred between 10 and 15 October at 22:00 h. Incident waves ranged from about 2.0 to 4.0 m. The sandbar migrated approximately 50 m offshore during this period.

3.2. Model forcing and input data

The hydrodynamic and morphological measurements used here are the same as those used previously (Gallagher et al., 1998). For each bar migration event, the 1-D model is forced with 2-Hz time series of horizontal water velocity measured by near-bottom-mounted current meters that extended from the shoreline to about 4.5 m depth (Fig. 2). During each migration event, the current meter height above the bed changed as the bed elevation changed. Thus, in the simulations, the water depth was updated every 3 h to account for tide excursion and wave setup, and the current meter height was adjusted to reflect the observed bottom changes (Fig. 2). In the bar trough, where the bottom erodes during offshore bar migration, the current meters were as much as 2 m above the seafloor at the end of some of the events (Fig. 2).

The alongshore currents observed with the current meters shown in Fig. 2, were small during the onshore bar migration,

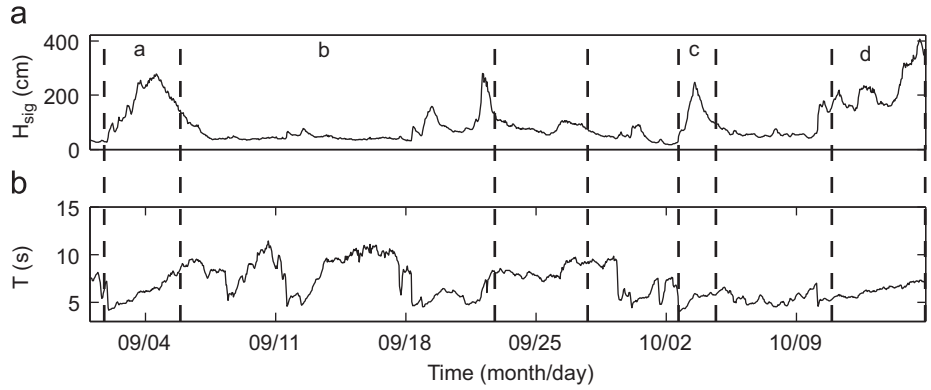

Fig. 1. (a) Significant wave height (H_{sig}) and (b) mean wave period (T, estimated from the centroid of the spectrum of sea-surface elevation between 0.05 and 0.30 Hz) observed in approximately 4 m depth versus time (date in 1994, EST). The four periods of interest are bounded by the dashed vertical bars, and labeled 'a', 'b', 'c', and 'd'.

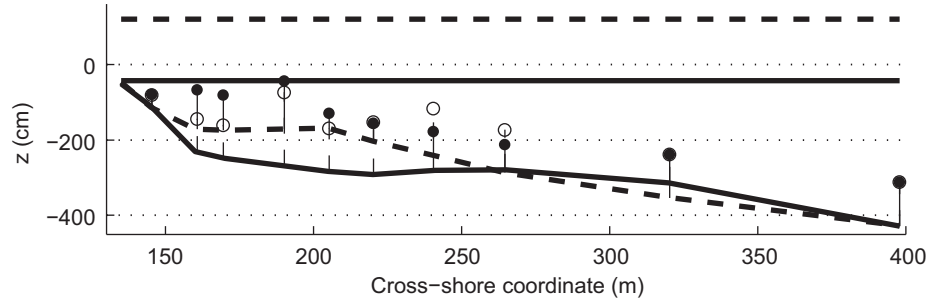

Fig. 2. Depth of the seafloor (dashed curve is 1 September, solid curve is 15 October), current meter locations (open and filled circles), and mean water levels at low (horizontal solid curve is 7 September at 13:00 h) and high (horizontal dashed curve is 15 October at 16:00 h) tides. The open and filled circles at each current meter location indicate the range of vertical positions for sensors that were raised or lowered in response to bar migration.

while cross-shore and temporal changes in alongshore currents were observed during the three offshore migration events. The greatest change occurred during event 'd', where the alongshore current across the region changed from about 1 m/s to the south at the beginning of the storm to about 1 m/s to the north just prior to the peak of the storm of 15 October.

In-situ mean sediment grain sizes ranged from 0.30 mm at the shoreline to 0.15 mm at water depths of about 5 m (Gallagher et al., 1998). Here, a constant value of 0.20 mm was used, consistent with previous studies on this beach (Thornton et al., 1996; Henderson et al., 2004; Hsu et al., 2006). The significance of neglecting apparently real variations in the cross-shore distribution of sediment size is not clear. Previous results suggest that a better prediction is obtained with a grain size distribution varying with the cross-shore location (Gallagher et al., 1998). However, the skill for predictions made with a variable settling velocity, although higher in every case, are not statistically different from the predictions made with constant grain sizes. Other previous results show that one event (1–5 September, event 'a') was reproduced better using a constant sediment diameter than with a variable size, whereas another event (2–4 October, event 'c') was reproduced better with variable grain sizes (Henderson et al., 2004). Here, a constant sediment diameter is chosen a priori, allowing focus to be on the sediment-induced stratification effects.

3.3. Numerical methods for the conservation of mass

Assuming that the divergence of the alongshore sediment flux is identically zero and the density of the sediment packing is constant, the mass conservation equation depends only on the cross-shore sediment transport rate (Thornton et al., 1996), and can be expressed as

$$\frac{dh}{dt} = \frac{1}{\mu}\frac{dQ_x}{dx} \tag{13}$$

where h is the bed elevation and μ is a packing factor (0.7) (Thornton et al., 1996). The net time-averaged and vertically integrated transport value Q_x is estimated here by vertical integration of the product of simulated sediment concentration and simulated cross-shore velocity at each current meter location. Time series were created from successive integrations over 512 s. Based on previous results (Thornton et al., 1996; Gallagher et al., 1998; Henderson et al., 2004) bed load is assumed negligible, and has been excluded from the simulations. Eq. (13) is solved using the SF08 numerical scheme reported in Appendix A.

The modeled transport rate at each location was partitioned into 'mean', 'infragravity' ($0.001 < f < 0.050$ Hz, where f is frequency), 'wave' ($0.050 < f < 0.300$ Hz), and 'net' contributions, the latter being the sum of the other three components. The 'wave' and 'infragravity' components are calculated from the product of the raw co-spectrum of concentration and cross-shore velocity (Conley and Beach, 2003), while the mean component is the product of the temporal mean of the concentration and the temporal mean of the cross-shore velocity. For each event, by band-pass filtering the time series Eq. (13) is used to estimate the bed elevation changes owing to these distinct sediment transport contributions.

4. Results

The model skill S is defined as (Henderson et al., 2004)

$$S = 1 - \frac{\sum_{i=1}^{N}(h_i^P - h_i^0)^2}{\sum_{i=1}^{N}(h_i^I - h_i^0)^2} \tag{14}$$

where h_i^P is the final predicted height of the seafloor, h_i^0 is the final observed height, h_i^I is the initial observed height, and N is the number of the locations at which the seabed height is estimated. If the model prediction were perfect, the skill would be equal to 1. If the model were more (less) accurate than the assumption of no change (S=0), then the skill would be positive (negative).

The inverse modeling discussed in Appendix A is used to indicate how well a model based on the spatially sparse measurements utilized here can be expected to reproduce the observations. In this respect, the bathymetric changes simulated using the inverse modeling based on the SF08 scheme are labeled as "prediction thresholds."

4.1. The offshore event 'a'

During this event, the approximately 50 m offshore migration that was observed is simulated accurately (S=0.60, see Table 1) by the model that includes buoyancy effects (SIS) (circles in Fig. 3a). Differences between model and data are within the range of the expected errors owing to finite difference techniques (prediction thresholds on the thin dotted curves in Fig. 3a, see Appendix A). For example, given the sparseness of the observations, inverse modeling (Appendix A) suggests an underestimation of the seabed erosion is likely to occur near the cross-shore position x=265 m as an artifact of the finite differencing.

Table 1
Model skill as defined in Eq. (14) for the complete profile predictions presented in Fig. 3.

	SIS γ_1	NSS γ_2	NSS γ_1
Case 'a'	0.60	0.51	0.23
Case 'b'	0.52	0.48	0.18
Case 'd'	0.44	0.66	0.68

The underestimation of the erosion observed onshore of the bar trough ($x<200$ m, Fig. 3a) is not owing to artifacts of finite differencing (the model predictions fall outside the prediction thresholds on the thin dotted curve in Fig. 3a), suggesting model errors, similar to previous results (Gallagher et al., 1998; Henderson et al., 2004; Hsu et al., 2006).

If stratification is neglected, while using the same model parameters (γ_1) as used in the SIS, the NSS model overpredicts (S=0.23, see Table 1) both the erosion observed for $200<x<220$ m and the accretion observed near x=265 m (squares) in Fig. 3a. Reducing the sediment concentration parameter (i.e., using γ_2=1.20e−03 instead of using γ_1=1.54e−03) improves the predictions (compare triangles with squares for $200<x<265$ m in Fig. 3a), but the transport divergence remains too large (S=0.51, see Table 1).

The transport partitioning during this event shows that the relative importance of the different components varies in the cross-shore (Fig. 4). In addition to previous results (Thornton et al., 1996; Gallagher et al., 1998) that showed mean-flow-driven sediment transport is important during offshore bar migration, the simulations with GOTM suggest that although mean-flow-driven transport may dominate on the seaward flanks of the bar ($270<x<320$ m) and trough ($175<x<220$ m), wave-driven transport may dominate on the landward flanks of the bar

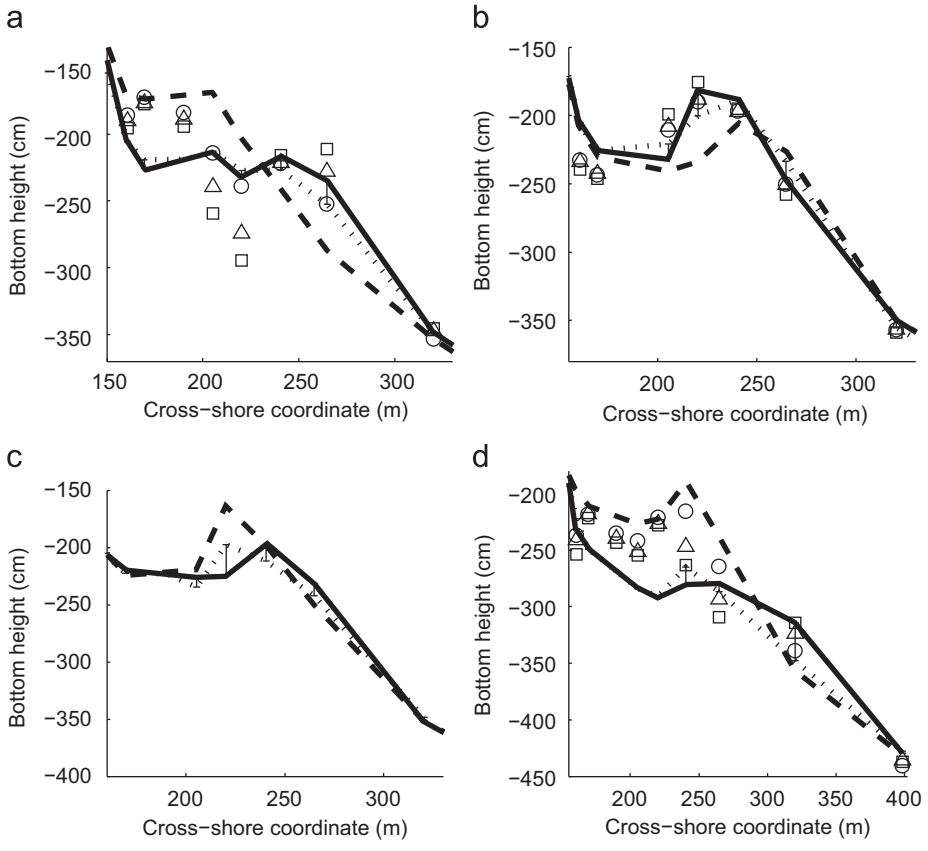

Fig. 3. Depth of the seafloor versus cross-shore coordinate for 4 sandbar migration events ('a', 'b', 'c', and 'd'). The dashed curves are the initial observed profiles, the thick curves are the profiles observed at the end of the event, and the thin dotted curves are the predictions of the final profile obtained through the inverse modeling (vertical lines are prediction thresholds owing to finite-difference techniques) (Appendix A). The circles are the predicted bed elevation at the end of the simulation with sediment stratification included. The squares (γ_1=1.54e−03) and triangles (γ_2=1.20e−03) are predicted bed elevations obtained by neglecting stratification. As discussed in the text, there are no model results for case 'c'.

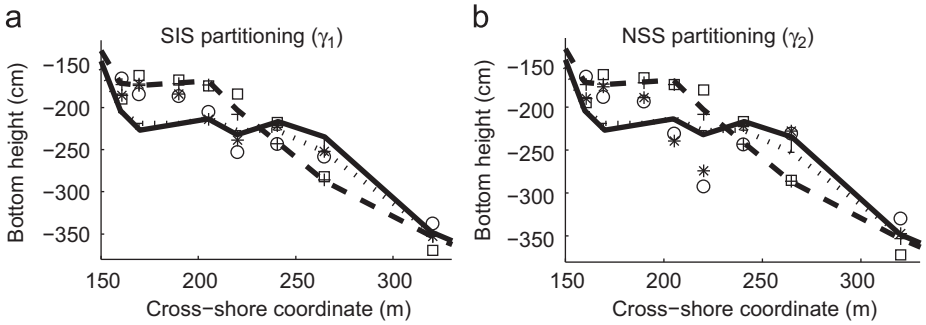

Fig. 4. Depth of the seafloor versus cross-shore coordinate for case 'a' (1–5 September). The dashed and solid curves are the original and final observed profiles, respectively. The thin dotted curves are the prediction obtained using inverse modeling (vertical lines are prediction thresholds). Panels (a) and (b) show results for the SIS (γ_1) and NSS (γ_2) cases, respectively. The symbols represent the contribution to the final profile prediction of mean (circles), infragravity (plusses), wave (squares), and net (stars) transport components.

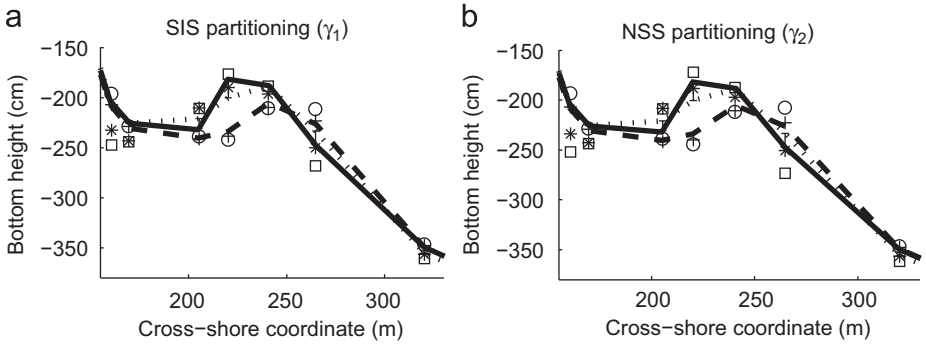

Fig. 5. Depth of the seafloor versus cross-shore coordinate for case 'b' (22–27 September). Format is the same as Fig. 4.

(x=240 m) and trough (x=165 m). The comparison with the NSS results demonstrates that although the wave transport component (squares in Fig. 4) remains unchanged between the two simulations, the mean component (circles in Fig. 4) increases strongly for the NSS solution.

4.2. The onshore event 'b'

During this event, the approximately 20 m onshore migration that was observed is simulated accurately (S=0.52, see Table 1) by the model that includes buoyancy effects (SIS) (Fig. 3b). Differences between model and data are consistent with expected errors owing to finite difference techniques (prediction thresholds on the thin dotted curves in Fig. 3b, see Appendix A), in particular the larger (than observed) accretion predicted near x=205 m and the smaller accretion predicted near x=220 m.

Using the same parameters as used with the SIS model (e.g., γ_1), the NSS solution simulates the accretion observed near the bar crest, but the skill is reduced artificially because of areas of little change. Predictions using the NSS model with the reduced calibration parameter (γ_2) are similar to those of the SIS model (compare triangles with circles in Fig. 3b). The similarity in SIS and NSS predictions suggests that during low-to-moderate wave conditions the prediction obtained using the SIS model is similar to that obtained by neglecting the sediment-induced buoyancy effects if the lower reference sediment concentration is accounted for. Thus, boundary layer processes dominate during the onshore bar migration observed in this case, as confirmed by the contributions of the different components (Fig. 5). The transport occurring near the bar-trough is almost entirely owing to the wave component (squares for $200 < x < 240$ min Fig. 5), while the mean (circles) and infragravity (plusses) components have

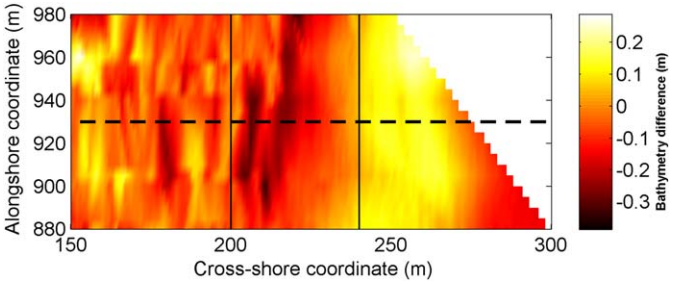

Fig. 6. Difference between the bathymetry surveyed on 3 October and the bathymetry surveyed on 4 October (case 'c'). The horizontal dashed line shows the location of the cross-shore transect of sensors (Fig. 3), and the two vertical solid lines indicate the region in which major alongshore changes in the bathymetry occurred.

smaller influence. Seaward of the bar crest, the mean-current induced component of transport counteracts the wave-driven transport. These model results are consistent with previous studies (Thornton et al., 1996; Gallagher et al. 1998; Henderson et al., 2004; Hsu et al. 2006) that suggest the observed net onshore sandbar migration was caused by the wave-induced component of transport.

4.3. The offshore event 'c'

Bathymetric surveys analyzed for the entire experiment (not shown) indicate significant alongshore gradients in transport during event 'c' only (Fig. 6), which violates the assumptions used to derive Eq. 13. Consequently, this event was not modeled. However, the inverse modeling (Appendix A) shows that large errors can be expected owing to finite difference effects

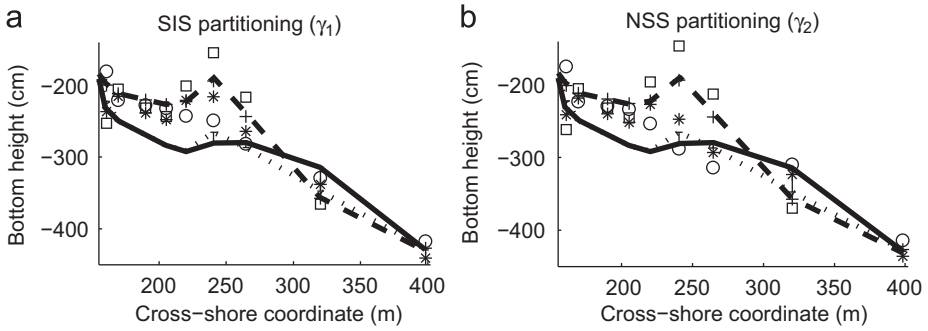

Fig. 7. Depth of the seafloor versus cross-shore coordinate for case 'd' (10–15 October). Format is the same as Fig. 4.

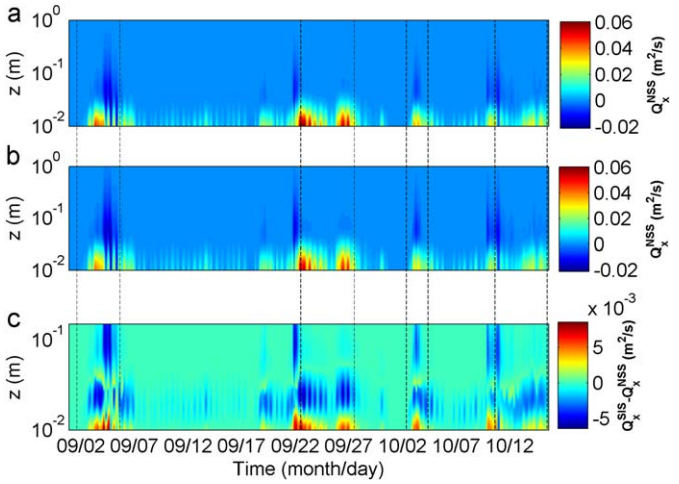

Fig. 8. The net transport rates ([m^2/s], color contours) as a function of depth above the seafloor (z, log scale) and time for 45 days at cross-shore location x=240 m simulated by the (a) SIS and (b) NSS models. The difference between the SIS and NSS transport predictions is shown in (c). The four sandbar migration events discussed in the text are between the vertical dashed lines.

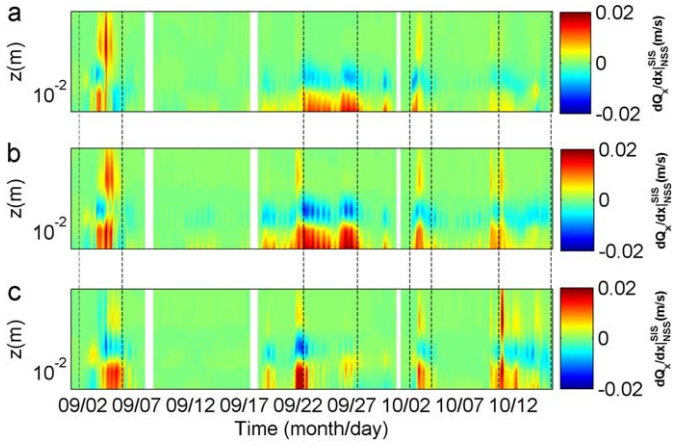

Fig. 9. Difference (SIS–NSS) in net transport divergence ([m/s], color contours) as a function of distance above the seafloor (z) and time. Cross-shore locations are (a) x=205, (b) x=220, and (c) x=245 m. The four sand bar migration events discussed in the text are between the vertical dashed lines.

(prediction threshold on the grey curve in Fig. 3c), possibly explaining the low skill of previous model predictions (Gallagher et al., 1998; Henderson et al., 2004). At best, simulations with the differencing scheme utilized here could reproduce one half of the measured erosion of this event.

4.4. The offshore event 'd'

During this event, the approximately 50 m offshore migration that was observed is simulated with a skill of S=0.44 by the model that includes buoyancy effects (SIS) (Fig. 3d, Table 1). In contrast, the NSS model (for either value of γ) has higher skill (S=0.66 and 0.68, Table 1). While the three models underpredict the erosion observed onshore of x=230 m, the higher NSS skill results from the better estimation of the morphological change offshore x=230 m (Fig. 3d). The inverse modeling technique suggests that a prediction of almost no change is likely to occur near x=320 m, consistent with the SIS results.

Although the circulation was complex, with alongshore mean currents across the surf zone changing from about 1 m/s to the south at the beginning of the storm to about 1 m/s to the north just prior to the peak of the storm on 15 October, alongshore divergences of sediment transport were small (Gallagher et al., 1998). The spatial distribution of the transport partitioning for this case (Fig. 7) is different from that observed during the offshore bar migration event 'a'. In case 'd' the wave component (squares in Fig. 7) is not negligible at any of the cross-shore locations considered, resulting in a net transport that is a balance between the wave and mean transport components.

The difference between the NSS and SIS solutions is mainly in the prediction of the magnitude of the 'mean' transport component offshore of approximately x=230 m (Figs. 3d and 8).

The failure in the estimate of the erosion rate within the trough ($220 < x < 265$ m, Figs. 3d and 8) appears to be owing to an underestimation of the mean-flow-driven transport in both the simulations.

5. Discussion

The 'net' transport rate as a function of vertical coordinate and time for the entire 45-day period at cross-shore location x=240 m is shown in Fig. 8. The change in direction of the transport in the vertical is evident in all cases. Within 3 or 4 cm of the bed, the transport is directed onshore (positive, red–yellow contours in Fig. 8), whereas at locations more than about 4 cm above the bed the transport is directed offshore (blue contours in Fig. 8). Moreover, the magnitude of the onshore transport usually is larger than that of the offshore transport (as much as a factor of 3) during periods characterized by low wave conditions (e.g., time=09/22–09/27 in Fig. 8a,b).

In the boundary layer near the seabed, the transport predicted by the model that includes buoyancy effects (SIS) is larger than the transport predicted by the model that ignores buoyancy effects (NSS) (Fig. 8c, red areas are where the difference between the two transport rates is positive). In the upper part of the water column, where, owing to the absence of turbulence damping, the

magnitude of the NSS transport is much larger than the transport predicted by the SIS solution. During periods of energetic forcing (e.g., 09/02–09/07, 10/10–10/12 in Fig. 8) the NSS model predicts high sediment transport rates at elevations as high as 1 m above the bed, whereas the SIS simulated rates are close to zero at elevations greater than about 0.6 m above the bed.

During onshore bar migration (case 'b') sediment transport takes place near the bed (09/22–09/27 in Fig. 8). Although the SIS and NSS skills for this event are similar to each other (Table 1), as are the corresponding predictions of wave-driven transport (Fig. 5), the vertical distribution of transport within about 5 cm of the bed differs significantly (Fig. 8c). The increased onshore transport in the bottom boundary layer predicted by the SIS model results in transport divergence rates (09/22–09/27 in Fig. 9a–c), which on a depth-averaged basis balance the more evenly distributed vertical transport profile predicted by the NSS model (Fig. 8b).

In contrast, there are large differences in mean-driven transport predicted by the SIS and NSS models for the offshore migration during event 'a' (compare circles in Fig. 4a with those in Fig. 4b), resulting in relatively poor predictions of the net change in bed elevation near x=240 m (Fig. 4b). The difference in the mean-flow-driven component is a result of the turbulence damping by the sediment stratification present in the SIS solution that limits the suspension of the sediment in the upper portion of the water column (Fig. 10). The mean TKE (normalized by the maximum observed value for this cross-shore station) of the NSS model is always greater than that of the SIS model during this event (Fig. 10a). These larger TKE values, particularly at the bottom, are caused by the absence of the buoyancy terms in the NSS solution. The sediment-induced buoyancy effect is confined to within a few centimeters of the bottom (Fig. 10b), constraining most of the suspended sediment concentration of the SIS solution into the boundary layer. In contrast, the sediment concentration simulated by the NSS solution is dispersed higher in the water column, explaining the larger near-bed SIS transport, and the greater NSS transport higher in the water column (Fig. 10d). The concentration at the bottom (lowest computation cell) is always larger for the SIS than for the NSS predictions (Fig. 10c), consistent with more onshore transport (Fig. 10) and greater transport divergence (Fig. 9) near the bottom in the SIS simulations than in the NSS simulations.

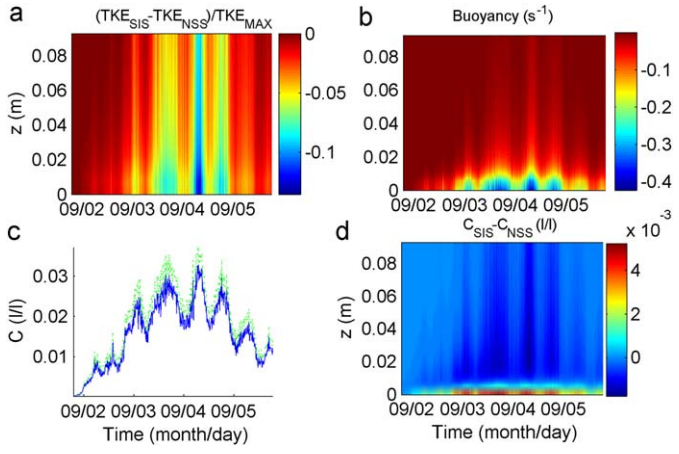

Fig. 10. (a) The vertical distribution of the difference between the SIS and NSS time series (SIS–NSS) of the 512-s dimensionless mean TKE and (b) the mean buoyancy production term [s^{-1}] for the SIS solution versus time. (c) The bottom sediment concentration [$l\,l^{-1}$] for the NSS (blue curve) and SIS (green curve) simulations versus time, and (d) the vertical distribution of the difference between SIS and NSS mean concentration versus time [$l\,l^{-1}$]. The cross-shore coordinate is x=220 m.

Thus, the different transport rates predicted by the SIS and NSS models in the upper part of the water column result from differences in bottom boundary layer processes. The NSS solution simulates an excess mass of sediment suspended into the upper part of the water column that is available to be transported by the undertow, leading to the larger, erroneous erosion rates predicted by the NSS model.

In contrast with the offshore migration in case 'a', the NSS model is more skillful than the SIS model for the offshore migration in case 'd' (Fig. 3). Onshore of the initial location of the bar crest location (x=200 m for 'a' and x=220 m for 'd'), SIS and NSS predictions are similar (Fig. 3a,d), and both underpredict the observed erosion. The reduced model skill onshore of the bar crest may be an artifact of driving the models with observations observed relatively far above the seabed (Fig. 2), possibly leading to inaccurate representations of the flow field. The main differences between SIS and NSS simulations during offshore migration are between the initial and final locations of the bar crest [$200 < x < 265$ m for 'a' (Fig. 3a) and $245 < x < 320$ m for 'd' (Fig. 3d)]. In this region, the SIS has more skill in 'a', and the NSS has more skill in 'd'. The increased skill of the NSS model predicting the offshore migration in event 'd' (e.g., x=245 m in Fig. 3d) can be explained by increased simulated mean-flow-driven transport divergence higher in the water column (Fig. 9c, time=10/10–10/15). This result contradicts the results for case 'a', and can be explained if the higher suspended transport simulated by the NSS models was fortuitously closer to the observations. The SIS solution constrains the suspended load to near the seabed owing to buoyancy effects, whereas in the surf zone additional, but unaccounted for sources of turbulence (e.g., turbulence injected into the water column from the surface by breaking waves and bores [Roelvink and Stive, 1989; Kobayashi and Johnson, 2001; Ogston and Sternberg, 2002; Feddersen et al., 2003]) may suspend sediment higher into the water column where it can be transported by mean currents. In this case, a model that erroneously simulates high levels of bed-generated turbulence would give the impression of being correct.

Differences in the location of the breaking region are consistent with the hypothesis that neglect of buoyancy compensates for neglect of breaking-induced turbulence during energetic conditions. The energy of the wave field during case 'd' was almost 3 times the energy during case 'a,' consistent with visual observations of a much more intense and wider surfzone in case 'd.' Moreover, the biggest differences between SIS and NSS simulations for case 'a' occur within the bar trough ($205 \le x \le 220$ m, Fig. 3a) where wave breaking is reduced. In contrast, the biggest differences between SIS and NSS simulations for case 'd' occurred near the bar crest ($241 \le x \le 265$ m, Fig. 3d) where wave breaking was most intense.

To estimate qualitatively the effect of externally generated turbulence on the vertical sediment concentration profile and subsequent transport, the SIS model was extended to inject a TKE flux (F_k) at the surface. The flux F_k is approximated by integrating in time and space the vertical turbulence production (PROD) owing to a surface roller appropriate for the spilling breakers observed during the field observations reported here (Eq. (4.73) in Fredsoe and Deigaard, 1992):

$$F_k = \int_0^T \int_{-H}^{0} \frac{PROD}{\rho} dz\,dt = \frac{gDH^3}{T(4D^2 - H^2)} \tag{15}$$

where T is the wave period, H and D are, respectively, the differences between the water depths at each side of the roller and the average water depth through it. Here, a wave group of 30 s duration, observed at x=240 m during the 11 October 04:00 h run was simulated. Taking a typical value for H/D of 0.5 and using

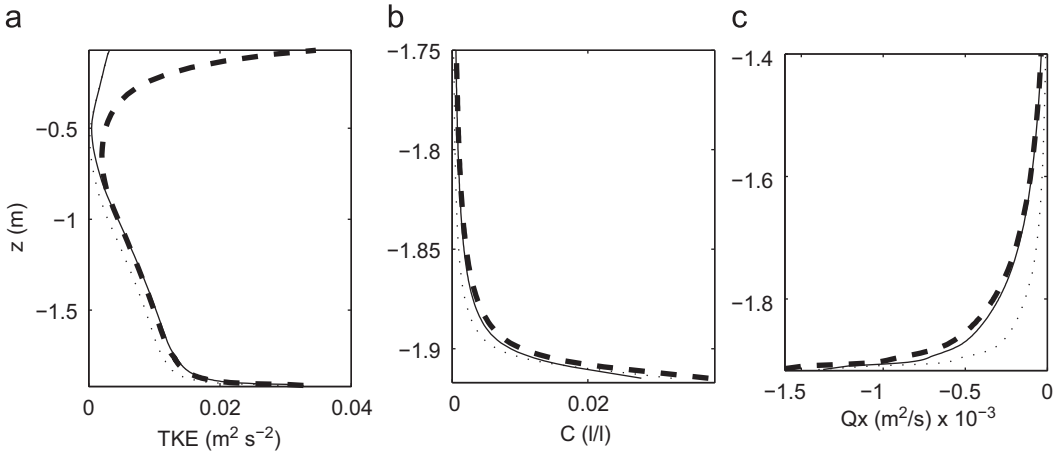

Fig. 11. (a) Mean vertical profile of the turbulent kinetic energy (TKE, [$m^2\ s^{-2}$]), (b) sediment concentration (C, [$l\,l^{-1}$]), and (c) cross-shore sediment transport (Q_x, [m^2/s]) during a wave group on 11 October 04:00 h at the cross-shore coordinate x=240 m. The light dotted and solid curves are results obtained with the standard SIS and NSS (γ_2) models, respectively, while the dashed curve is the SIS model including an artificial TKE flux at the surface.

for D the observed mean water depth of 2 m, a TKE flux of 0.26 m^3/s^3 is obtained during the estimated wave period of 5 s. The appropriate fraction of this flux is injected at each time step by means of the surface boundary condition for the TKE. A different boundary condition for the dissipation rate, which follows from assuming a power law decay for the TKE at the surface, as observed in grid stirring experiments (Umlauf et al., 2003) is used in this case.

The mean vertical TKE profile of the SIS solution with inclusion of F_k matches the NSS solution below about 0.8 m beneath the surface (Fig. 11a), whereas the pure SIS solution contains significantly less TKE throughout the majority of the water column. Consequently, the SIS solution with F_k included exhibits a greater suspended sediment load above the near bed region than predicted by the pure SIS solution (Fig. 11b). This difference results in the prediction of greater offshore sediment transport than is observed in the absence of the surface-generated turbulence (Fig. 11c). The transport for the NSS simulation (without the inclusion of F_k) is similar to that from the SIS simulation including surface-generated turbulence (Fig. 11c).

The spatial distribution of transport partitioning for case 'd' would be affected both for SIS and NSS solutions when including externally generated turbulence. Whereas the wave-induced transport component is thought to remain unaltered unless breaking-induced turbulence penetrates near the bed, the mean component would increase significantly both for SIS and NSS solutions. However, the wave-induced transport seaward and landward of the bar crest would remain significant (Fig. 7). Although there are no wave-resolving simulations of event 'd' available for a comparison, similar to results from phase-averaged simulations (Hoefel and Elgar, 2003; Hsu et al., 2006), the model results suggest that the wave-induced component of transport is important for both of the offshore bar migration events ('a' and 'd') simulated.

6. Conclusions

Nearshore sandbar migration observed on an ocean beach was simulated with the k–ε turbulence module of a 1-D General Ocean Turbulence Model (GOTM) that includes the effects of sediment-induced stratification. Contrary to most previous studies of sandbar migration, the simulations presented here do not rely on the adjustment of tunable parameters for different runs. The two free model parameters, the bed reference concentration and sediment diffusivity, have been calibrated independently with field observations obtained from the same beach, but 3 years later.

Considering both onshore and offshore migration, the model that includes sediment-induced stratification (SIS) had higher skill than the model without stratification (NSS). Differences in the sediment transport patterns simulated by the SIS and NSS solutions occur throughout the water column, although the apparent net transport differences are predominantly owing to the mean-flow-induced transport component higher in the water column. In contrast with the non-stratified NSS model, buoyancy effects in the SIS model damp turbulent kinetic energy in the boundary layer, and thus restrict suspended sediment from rising more than a few cm above the seafloor. Opposing differences in the wave-driven transport in the lower part of the water column result in similar transport divergences predicted by the models near the bed. For example, although there is a considerable difference in the vertical distribution of modeled sediment transport during onshore bar migration (during which wave-driven transport dominates), the SIS and NSS models have similar skill.

Consistent with previous results, onshore sandbar migration is driven by the wave-induced component of transport. In addition, the simulations here suggest that both mean-flows (similar to previous results) and waves are important to offshore bar migration. Wave-driven transport was found to dominate on the landward flanks of both the bar and the trough during a moderately energetic storm, and both seaward and landward of the bar crest during the most energetic waves observed.

Although the SIS model has higher skill than the NSS model on average, there are cases for which neglecting stratification results in better predictions. These cases primarily occur during the most energetic waves, and may be an artifact of neglecting breaking-wave-induced turbulence that in reality results in more sediment suspended high in the water column than predicted by the damped turbulence near the bed in the SIS model. Inclusion of the effects of surface-generated turbulence, along with the effects of sediment-induced turbulence damping in the bed boundary layer, results in further improvements of the SIS model.

Acknowledgements

We thank R.T. Guza, E.L. Gallagher, and B. Raubenheimer, and the staff of the US Army Corps of Engineers Field Research Facility in Duck, NC for helping obtain the field observations, which were funded by the US Office of Naval Research and the US National

Science Foundation. We thank S.M. Henderson for providing information about the altimeter depths and for discussing mechanisms for shoreward sandbar migration. The NATO Undersea Research Centre, the D.I.C.A.T. of Genova University, the US Office of Naval Research, and the US DoD NSSEFF program sponsored this research.

Appendix A. Finite differencing

The collocated current meters and altimeters were unequally spaced in the cross-shore direction (Fig. 2), requiring specific spatial differencing methods to estimate the transport divergence accurately. In the past, several approaches have been used (Gallagher et al., 1998 (hereinafter GL98), Plant et al., 2004 (hereinafter PT04), a simple method obtained from Taylor's series (hereinafter TY1), and the one employed here (hereinafter SF08) (see Appendix B). To compare the different approaches, an inverse method is developed by first creating a continuous beach profile through linear interpolation of the bed elevations measured by 10 unequally spaced altimeters. Then, Eq. (13) is applied in a inverse manner to arrive at a continuous (1 m spacing) cross-shore transport rate. Lastly, Eq. (13) is applied using these "perfect" transport rates at the original measurement point to estimate directly the morphological change in the cross-shore direction, using the different transport gradients formulations (see Appendix B, Eqs. (B3)–(B6)). The availability of the nearly continuous in space (1 m spacing) bathymetry recorded by the Coastal Research Amphibious Buggy (CRAB) allows for a validation of the inverse modeling technique based on the data from the spatially sparse altimeters.

The transport divergence estimated with the differential methods is smoother than the observed divergence, owing to the spatial sparseness of the simulated altimeter stations (Fig. A1, especially panel f). While the SF08, GL98, and TY1 methods have similar divergences in all cases, occasionally the PT04 method predicts significantly different transport gradients (e.g., x=265 m in Fig. A1d).

Observed and predicted bathymetric changes obtained using the various differencing schemes at each cross-shore station are shown in Fig. A2. The bathymetric changes surveyed from the CRAB are not exactly the same as those reported by the altimeters (compare blue curves in the upper panels with the blue curves in the lower panels of Fig. A2). Despite these differences, the bathymetric changes predicted by the different methods have similar trends regardless of whether profiles are from the CRAB or the altimeters, implying that linear interpolation of the beach profile between pairs of altimeters does not undermine the inverse modeling technique.

The stability of each numerical scheme is tested with four different transport patterns (monotonically increasing, decreasing, convex, and concave shape) between a central station and the two adjacent points to the right and left side. Then by keeping the $p[=(x_{i-1}-x_i)]$ spacing constant (20 m) and increasing $q[=(x_{i+1}-x_i)]$ monotonically at one station (from 20 to 40 m), and vice versa, a normalized profile error (NPE) in the prediction of the bed elevation change can be estimated as a function of the spacing between the left and the right station:

$$NPE = \frac{(\Delta h)^0 - (\Delta h)^p}{(\Delta h)^0} \tag{A1}$$

where $(\Delta h)^0$and $(\Delta h)^p$ are the observed and estimated elevation changes, respectively.

This operation was performed for all the cross-shore stations, one by one, for all the beach profile variations observed. The NPE at four representative cross-shore positions is shown in Fig. A3. The PT04 method (green in Fig. A3) is much more sensitive to changes in both p and q than the other models are, and has relatively high NPE, regardless of the pattern of transport. Overall, the SF08 method has the smallest NPE, but GL98 and TY1 schemes (with similar NPE) are included in the analysis.

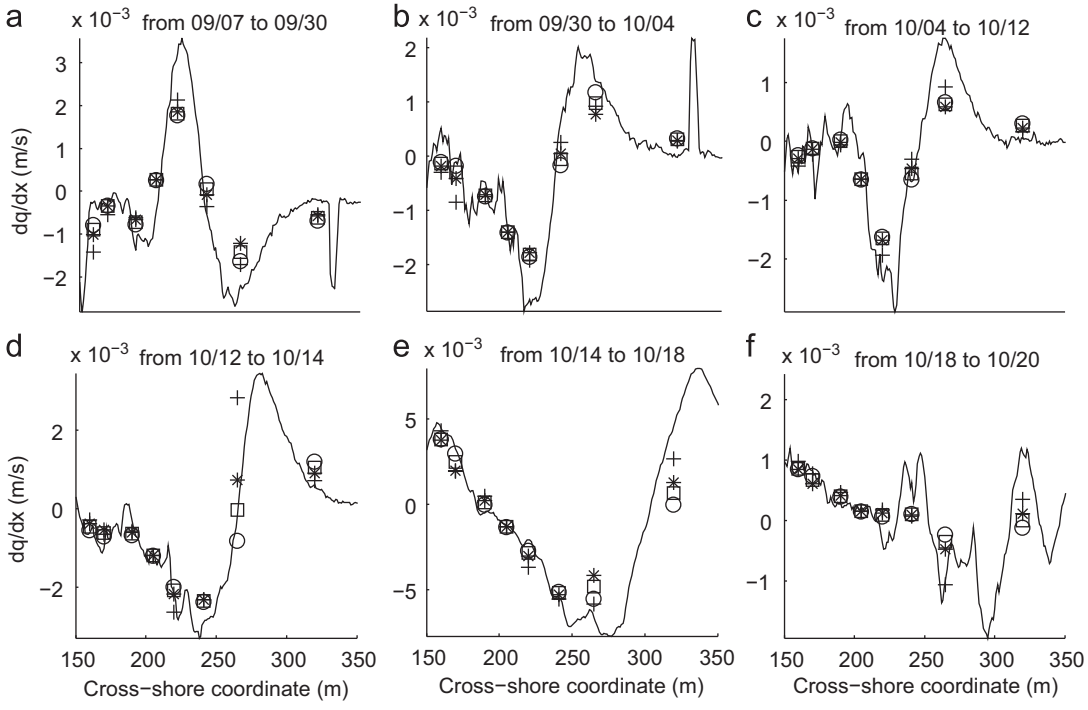

Fig. A1. Transport gradient versus cross-shore coordinate. Gradients were estimated by CRAB surveys (solid curves), and by the SF08 (circles), PT04 (plusses), GL98 (squares), and TY1 (stars) differencing schemes. Panels a–f refer to different time periods (labeled above each panel).

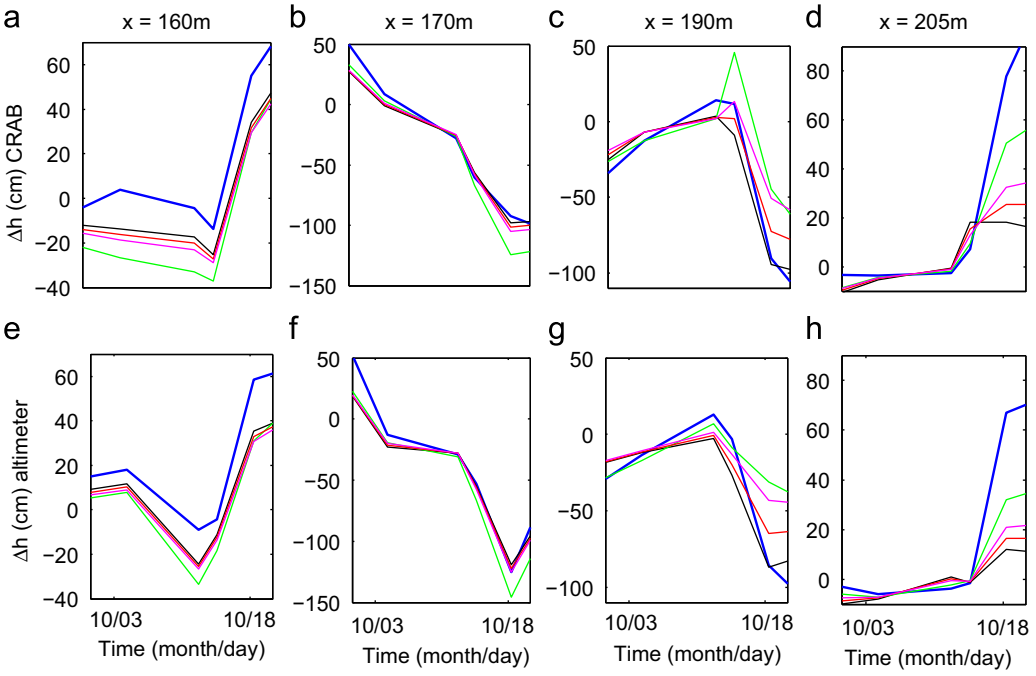

Fig. A2. Change in bed elevation obtained by inverse modeling versus time for different finite difference schemes. The thick blue curves are based on linear interpolation of observed profiles (a–d are based on CRAB surveys, e–h are based on altimeter data), and the finite-difference estimates are SF08 (black curves), GL98 (red), TY1 (magenta), and PT04 (green).

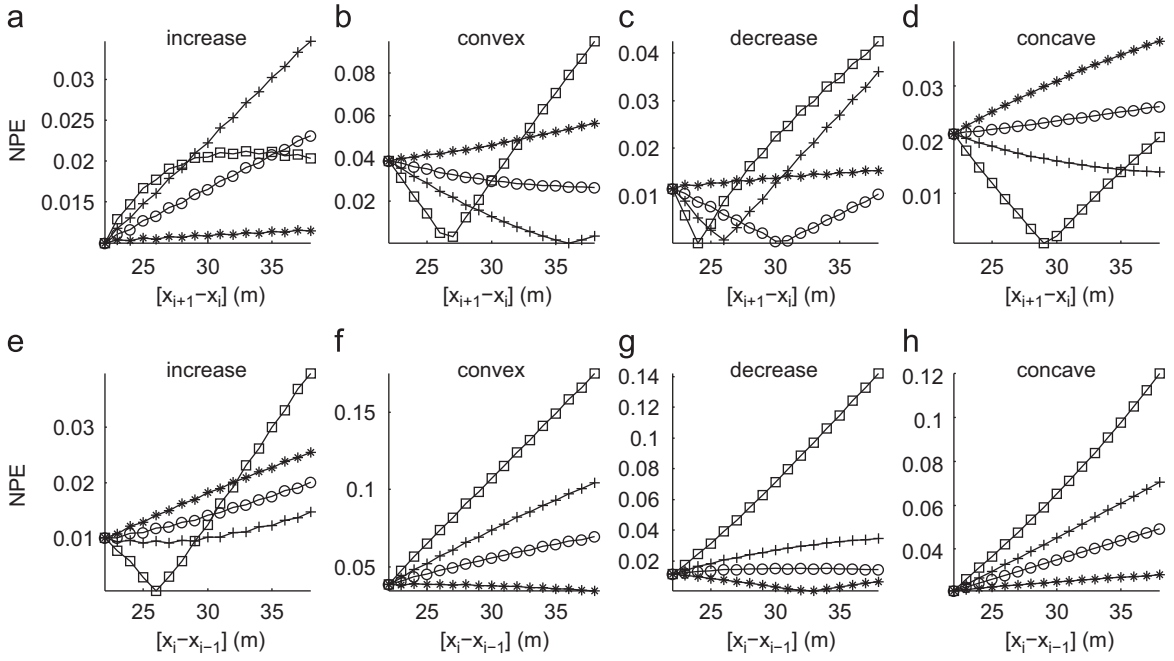

Fig. A3. (a–d) NPE versus $x_{i+1}-x_i$ and (e–h) NPE versus x_i-x_{i-1} at a single cross-shore location while keeping $(x_{i-1}-x_i)$ constant (top panels) and while keeping $(x_{i+1}-x_i)$ constant (bottom panels) for the TY1 (plusses), GL98 (circles), PT04 (squares), and SF08 (stars) finite difference schemes.

The observed (with altimeters) and predicted bathymetric changes at each cross-shore station derived using three of the differencing schemes are shown in Fig. A4. Even using a perfect transport rate, the numerical predictions are fairly inaccurate at some stations (e.g., x=265 and 320 m), suggesting that interpolation of the observations combined with artifacts of finite differencing may degrade model simulations. The associated prediction errors are shown as vertical bars in Figs. 4–6 and 8.

An overall root mean-square error in the prediction (RMSEP) at each cross-shore station can be estimated as

$$RMSEP = \sqrt{\sum_{i=1}^{n} \left(NPE|_i\right)^2 / n} \tag{A2}$$

where n represents all the time steps considered. The GL98 ($RMSEP$=0.344), TY1 ($RMSEP$=0.361), and SF08 ($RMSEP$=0.341) methods are similar (Fig. A4), and SF08 is used here.

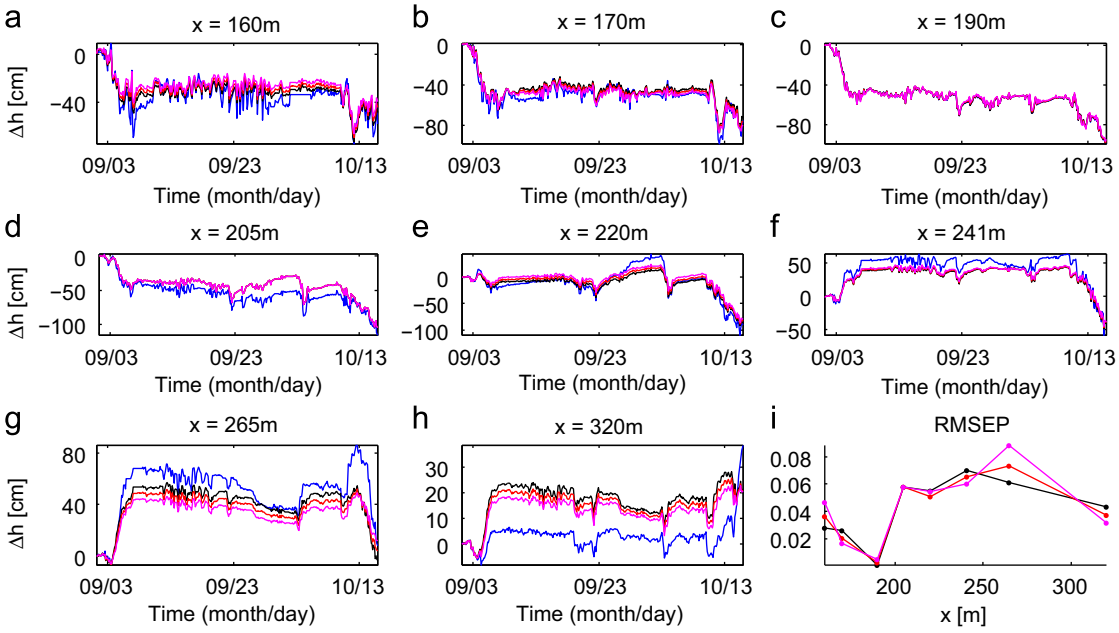

Fig. A4. Change in bed elevation versus time at each cross-shore station (locations are above each panels) as observed (blue curves) and obtained by inverse modeling for the SF08 (black), GL98 (red), and TY1 (magenta) differencing methods. (i) RMSEP versus cross-shore location for each method.

Appendix B. Numerical schemes

In the case of non-uniform grid spacing where q and p represent the forward and backward spacing, respectively, the forward and backward differences, respectively can be expressed as

$$f'(x) = \frac{f(x+q)-f(x)}{q} + O(q) \tag{B1}$$

$$f'(x) = \frac{f(x)-f(x-p)}{p} + O(p) \tag{B2}$$

Thus, the first-order accurate (in space) method TY1, may be obtained by subtracting Eqs. (B1) and (B2):

$$f'(x) = \frac{f(x+q)-f(x-p)}{(q+p)} + \mathrm{O}(q-p) \tag{B3}$$

The PT04 method and GL98 methods are described in the appendix of Plant et al. (2004). The GL98 method is the average of backward and forward differences, thus obtained from the sum of Eqs. (B1) and (B2) as

$$f'(x) = \frac{f(x+q)-f(x)}{2q} + \frac{f(x)-f(x-p)}{2p} \tag{B4}$$

The PT04 method is a weighted average of backward and forward differences, which can be rewritten for comparison purposes as

$$f'(x) = \frac{q}{p(q-p)}\left[f(x+q)-f(x)\right] + \frac{p}{q(q-p)}\left[f(x)-f(x-p)\right] \tag{B5}$$

The alternate method proposed here, named SF08, is

$$f'(x) = \frac{p}{q(q-p)}\left[f(x+q)-f(x)\right] + \frac{q}{p(q-p)}\left[f(x)-f(x-p)\right] \tag{B6}$$

The difference between PT04 and SF08 is that the weights are inverted in the average of the backward and forward difference. The consequence is that the PT04 method puts the largest weight on the transport at the most distant location because that distance spans more space. In contrast, both SF08 and GL98 put the larger weight on the closer location, assuming it is more representative of the true difference. Thus, the weighting for the transport at the central location has opposite sign in the different cases. In the case of equal spacing, all methods are equivalent.

References

Bagnold, R.A., 1966. An approach to the sediment transport problem from general physics. Prof. Paper 422-I, US Geol. Surv.

Bailard, J.A., 1981. An energetics total load sediment transport model for a plane sloping beach. J. Geophys. Res. Oceans 86, 10,938–10,964.

Bailard, J.A., Inman, D.L., 1981. An energetics bedload transport model for a plane sloping beach: local transport. J. Geophys. Res. Oceans 86, 2035–2043.

Blackford, J.C., Allen, J.I, Gilbert, F.L., 2004. Ecosystem dynamics at six contrasting sites: a generic modelling study. J. Mar. Syst. 52 (1–4), 191–215.

Bowen, A.J., 1980. A simple model of nearshore sedimentation: beach profiles and longshore bars. Coastline Canada, Geol. Survey Canada, 1–11.

Burchard, H., Petersen, O., Rippeth, T.P.,J.I, 1998. Comparing the performance of the Mellor-Yamada and the k-epsilon two-equation turbulence models. J. Geophys. Res. 103 (C5), 10,543–10,554.

Burchard, H., Bolding, K., Villarreal, M.R., 1999. GOTM, a general ocean turbulence model, theory, implementation and test cases. Report EUR 1874, European Commission, 103pp.

Conley, D.C., Beach, R.A., 2003. Cross-shore sediment transport partitioning in the nearshore during a storm event. J. Geophys. Res. Oceans 108 (C3), 3065, doi:10.1029/2001JC001230.

Conley, D.C., Falchetti, S., Lohman, I.P., Brocchini, M., 2008. The effects of flow stratification by noncohesive sediment on transport in unsteady flows. J. Fluid Mech. 610, 43–67, doi:10.1017/S0022112008002565.

Drake, T.G., Calantoni, J., 2001. Discrete particle model for sheet flow sediment transport in the nearshore. J. Geophys. Res. Oceans 106, 19,859–19,868.

Elgar, S., Gallagher, E.L., Guza, R.T., 2001. Nearshore sandbar migration. J. Geophys. Res. Ocean 106 (C6), 11,623–11,628.

Feddersen, F., Gallagher, E.L., Guza, R.T., Elgar, S., 2003. The drag coefficient, bottom roughness, and wave breaking in the nearshore. Coast. Eng. 48, 189–195.

Foster, D.L., Bowen, A.J., Holman, R.A., Natoo, P., 2006. Field evidence of pressure gradient induced incipient motion. J. Geophys. Res. Oceans 111, C05004, doi:10.1029/2004JC002863.

Fredsoe, J., Deigaard, R., 1992. Mechanics of Coastal Sediment Transport. Advanced Series on Ocean Engineering, vol. 3. World Scientific Publishing, Singapore.

Gallagher, E.L., Elgar, S., Guza, R.T., 1998. Observation of sand bar evolution on a natural beach. J. Geophys. Res. Oceans 103, 3203–3215.

Glenn, S.M., Grant, W.D., 1987. A suspended sediment stratification correction for combined wave and current flows. J. Geophys. Res. Oceans 92 (C8), 8244–8264.

Henderson, S.M., Allen, J.S., Newberger, P.A., 2004. Nearshore sandbar migration predicted by an eddy-diffusive boundary layer model. J. Geophys. Res. Oceans 109, C06024, doi:10.1029/2003JC002137.

Hoefel, F., Elgar, S., 2003. Wave-induced sediment transport and sandbar migration. Science 299, 1885–1887.

Hsu, T.-J., Elgar, S., Guza, R.T., 2006. Wave-induced sediment transport and onshore sandbar migration. Coast. Eng. 53, 817–824.

Hsu, T.-J., Jenkins, J.T., Liu, P.L.-F., 2003. On two-phase sediment transport: dilute flow. J. Geophys. Res. Ocean 108 (C3), 3057, doi:10.1029/2001JC001276.
Jensen, B.L., Sumer, B.M., Fredsoe, J., 1989. Turbulent oscillatory boundary layers at high Reynolds number. J. Fluid Mech. 206, 265-297, doi:10.1017/S0022112089002302.
Kobayashi, N., Johnson, B.D., 2001. Sand suspension, storage, advection, and settling in surf and swash zones. J. Geophys. Res. Oceans 106, 9363–9376.
Munk, W.H., Anderson, E.R., 1948. Notes on the theory of the thermocline. J. Mar. Res. 3, 276–295.
Nielsen, P., 1992. Coastal bottom Boundary Layers and Sediment Transport. Advanced Series on Ocean Engineering, vol. 4. World Scientific Publishing, Singapore.
Nielsen, P., Teakle, I.A.L., 2004. Turbulent diffusion of momentum and suspended particles: a finite-mixing-length theory. Phys. Fluids 16 (7), 2342–2348.
Ogston, A.S., Sternberg, R.W., 2002. Effect of wave breaking on sediment eddy diffusivity, suspended-sediment and longshore sediment flux profiles in the surf zone. Continental Shelf Res. 22, 633–655.
Plant, N.G., Holland, K.T., Puleo, J.A., Gallagher, E.L., 2004. Prediction skill of nearshore profile evolution models. J. Geophys. Res. Oceans 109, C01006, doi:10.1029/2003JC001995.
Ralston, D.K., Stacey, M.T., 2006. Shear and turbulence production across subtidal channels. J. Mar. Res. 64 (1), 147–171.
Rodi, W., 1980. Turbulence Models and Their Applications in Hydraulics – A State of the Art Review. International Association for Hydraulic Research, Delft, The Netherlands.
Rodi, W., 1987. Example of calculation methods for flow and mixing in stratified fluids. J. Geophys. Res. (C5), 92, 5305–5328.
Roelvink, J.A., Stive, M.J.F., 1989. Bar generating cross-shore flow mechanisms on a beach. J. Geophys. Res. Oceans 94, 4785–4800.
Smith, J.D., McLean, S.R., 1977. Spatially averaged flow over a wavy surface. J. Geophys. Res. Oceans 82, 1735–1746.
Stips, A., Burchard, H., Bolding, K., Eifler, W., 2002. Modelling of convective turbulence with a two-equation k–e turbulence closure scheme. Ocean Dynam. 52 (4 doi:10.1007/s10236-002-0019-2.
Sumer, B.M., Kozakiewicz, A., Fredsoe, J., Deigaard, R., 1996. Velocity and concentration profiles in sheet-flow layer of movable bed. J. Hydr. Eng. ASCE 122 (10), 549–558.
Styles, R., Glenn, S.M., 2000. Modeling stratified wave and current bottom boundary layers on the continental shelf. J. Geophys. Res. Oceans 105 (C10), 24,119–24,139.
Thornton, E.B., Humiston, R.T., Birkemeier, W., 1996. Bartrough generation on a natural beach. J. Geophys. Res. Oceans 101, 12,097–12,110.
Trowbridge, J., Young, D., 1989. Sand transport by unbroken waves under sheet flow conditions. J. Geophys. Res. Oceans 94, 10,971–10,991.
Umlauf, L., Burchard, H., Hutter, K., 2003. Extending the $k-\omega$ turbulence model towards oceanic applications. Ocean Model. 5, 195–218.
Umlauf, L., Burchard, H., Bolding, K., 2006. GOTM Sourcecode and test case documentation. 1–231pp., Version 3.2, ⟨http://www.gotm.net⟩.